Universal Fourier optics model for virtual coherence scanning interferometers

Peter Lehmann, Tobias Pahl, and Jörg Riebeling

Measurement Technology, Faculty of Electrical Engineering and Computer Science,
University of Kassel, Wilhelmshoeher Allee 71, Kassel 34121, Germany

ABSTRACT

Optical surface topography measurements sometimes suffer from systematic errors. In order to predict such deviations, modeling of optical profilers is a substantial part of the European project TracOptic (Traceable Optics). Within the framework of this project, we recently developed the UFO (Universal Fourier Optics) model, which simulates virtual CSI measurements of surface topographies that fulfill the requirements of the scalar Kirchhoff approximation. The model enables a fast computation of 'measured' surface topographies as it is based on discrete Fourier transforms. It treats the surface under investigation as a two-dimensional phase object assuming a linear dependence of the interference phase on surface height and axial spatial frequency. The scattered light field is transferred to the Fourier domain and multiplied by a partial two-dimensional transfer function (TF) representing a horizontal cross section of the three-dimensional TF at a certain axial spatial frequency or evaluation wavelength, respectively. The TF includes parameters of the interference microscope and the reference field distribution. Inverse Fourier transform enables the reconstruction of the phase object. The coherence peak position of an interference signal results from numerical differentiation with respect to the axial spatial frequency and is generally used to overcome the 2π ambiguity of the phase profile. Parameters affecting final results of reconstructed surface topographies are the central wavelength and the spectral bandwidth of the illuminating light as well as the numerical aperture of the objective lens and the chosen evaluation wavelength. We discuss results of the UFO model with respect to the prediction of systematic deviations of measured surface topographies.

Keywords: Coherence scanning interferometry, Kirchhoff diffraction theory, Transfer function, Phase objects

1. INTRODUCTION

Coherence scanning interferometry (CSI) is a widely used optical topography measurement technique due to its outstanding axial resolution. Common configurations of CSI instruments are Michelson, Mirau and Linnik interference microscopes.[1] Light from the spatially extended source is split into two separate arms and focused to the measurement object and the reference mirror, respectively. The reflected light is then recombined such that the object and reference waves interfere and an interference pattern is recorded in the image plane of the microscope. In CSI systems typically either the measurement object or the reference mirror is scanned along the optical axis through the focus of the microscope objective. The optical path length difference of the two interferometer arms determines the phase of the interference signals that are recorded at each pixel of the camera. While temporally perfectly coherent light and a single angle of incidence causes a sinusoidal interference signal, a limited coherence length and a broad range of incidence angles leads to an envelope, which shows its maximum when both, the measurement object and the reference mirror are in focus of the objective lenses and the optical path lengths of the two interferometer arms are balanced. The coherence length and the depth of field depending on the numerical aperture (NA) of the system affect the width of signal envelope, as it is discussed in detail by Abdulhalim.[2] After signal acquisition the envelope position is typically estimated for each pixel separately to reconstruct the 3D topography. Today's CSI systems commonly use extended spatially incoherent light emitted by LEDs in a Köhler illumination arrangement.

Further author information:
Peter Lehmann: E-mail: p.lehmann@uni-kassel.de

Modeling Aspects in Optical Metrology IX, edited by Bernd Bodermann, Karsten Frenner,
Proc. of SPIE Vol. 12619, 126190O · © 2023 SPIE · 0277-786X
doi: 10.1117/12.2673292

In addition to the envelope, the phase of CSI signals provides information that enables an improved measurement accuracy. However, the phase values suffer from the 2π-ambiguity and thus need additional fringe order information or phase unwrapping procedures to recover the correct height data.

Even though CSI is considered to be one of the most powerful optical topography measurement methods it has to deal with systematic errors and limitations. Since conventional microscopic imaging is used to obtain interference patterns, the diffraction limit found by Ernst Abbe applies to the interferometric imaging process, too. In addition, systematic deviations like the batwing effect[3–6] or slope effects[7] that mainly affect the envelope position can lead to erroneous height values. To achieve the best possible measurement accuracy, these effects have to be kept in mind when evaluating CSI image stacks.

To fully understand these limitations and to predict the surface transfer characteristics of an optical system, the transfer function (TF) of the system has proven to be essential. In order to model the 3D image formation process of CSI systems, the three-dimensional transfer function (3D TF) has to be taken into account.

The surface of the object can be introduced as a thin foil, which is mathematically represented by a set of Dirac delta functions at certain height values.[8] The Fourier transform of the foil representation[9–13] of a surface with respect to the height (z) coordinate results in the so-called phase object representation of the electric field on the surface, where the term 'phase object' means an object that modulates the phase of an incident wave.[8,14] Thus, the phase object represents a fully equivalent approach to obtain the scattered light field and in contrast to the foil model only a 2D Fourier transform with respect to x and y coordinates is needed. A simulated image stack then follows from an inverse 3D Fourier transform of the product of 2D Fourier transformed phase objects for certain fringe frequencies and the 3D TF in the spatial frequency domain. On the other hand, if interference signals can be analyzed at a single fringe frequency. In this case one or two inverse 2D Fourier transforms of the product in the 3D spatial frequency domain enable the reconstruction of the input surface. This kind of CSI modeling is what we call the 'Universal Fourier Optics' model (UFO). If a certain average wavelength called equivalent wavelength, which corresponds to the most dominant interference fringe frequency, is used and the 2D Fourier transform of the corresponding phase object is low-pass filtered in the lateral spatial frequency plane by the MTF (modulation transfer function), which is well-known from 2D imaging, the results correspond to the elementary Fourier optics (EFO) model introduced by de Groot et al.[15] The EFO model uses the fact that under certain conditions an integration of the 3D TF agrees with the MTF defined in the 2D spatial frequency domain. However, the EFO model lacks accuracy at high NA values and if the envelope of the resulting interference signals is to be taken into account. The UFO model is based on previous investigations published in recent years.[16–19]

In addition to a fast computation of simulated CSI measurement results, analysing the 3D TF and the interference signals in the spatial frequency domain gives insight into the signal formation process and helps choosing most appropriate parameters for signal analysis. This is especially important when phase analysis is performed since this can be done for different frequency components of the interference signal. These frequency components carry information from different spatial frequencies of the object's surface,[16,20] so that analyzing the interference signal at an optimum fringe frequency is quite essential in order to achieve minimum deviation between the surface topography of the measuring object and the topography reconstructed by the CSI instrument.

2. THEORY

The theoretical treatment starts with CSI signal analysis in order to identify the minimum information that is needed in order to reconstruct a surface profile. Based on these results the second subsection introduces the way how the UFO model provides this information. The final subsection gives insight into the optical 3D TF.

2.1 Extended signal analysis in coherence scanning interferometry

To introduce the concept of extended signal analysis, Figures 1 (a) to (c) show simulated CSI signals for different positions along the z-axis representing the height of an object point. Note that at the position $z = 0$ the interferometer is balanced and thus the corresponding signal in Figure 1 (b) shows axial symmetry. The lower subfigures display the spectral magnitude and the phase spectra of the corresponding z-dependent signals including the individual sampling points along the fringe frequency f_z axis. Obviously, the spectral magnitude is independent of the height position of a signal. The density of sampling points in the frequency domain depends reciprocally

on the total scanning range of the depth scan along the z-axis. Comparing the phase spectra for different z-axis positions of the signal shows two characteristic properties. First, the absolute value of the phase for a certain fringe frequency depends linearly on the z-position of the signal. Unfortunately, due to the 2π-ambiguity the measured phase values are restricted to an interval of 2π in practice. However, if in addition the slope of the phase along the fringe frequency is considered, the 2π-ambiguity can be overcome enabling an unambiguous profile reconstruction. This is the basic idea of the FDA algorithm introduced 30 years ago by de Groot et al.[21,22] However, the envelope position results from the slope of the phase with respect to the fringe frequency. According to Figure 1 this slope shows a linear behaviour. Hence, an unambiguous profile reconstruction can be achieved by phase analysis at two different discrete phase values only. If the phase gradient is analyzed for two neighboring phase values corresponding to slightly different fringe frequencies separated by Δf_z, this leads to a total number of $n_{\max} - n_{\min} - 1$ different envelope profiles, where $n_{\max}$ and $n_{\min}$ are defined in Figure 1 (b). Of course, the total number of reconstructed individual phase profiles is then $n_{\max} - n_{\min}$. Each phase profile reconstruction is based on two 2D Fourier transforms of the field modulated by a phase object.

$$U_F(x,y) = U_{F0}\, \mathrm{e}^{-\mathrm{i}q_z h_{\mathrm{ph}}(x,y)} \tag{1}$$

represents the filtered complex-valued electric field of amplitude U_{F0} in the image plane (xy-plane) related to the angular fringe frequency $q_z = 2\pi f_z$. The filter characteristics depend on the properties of the optical imaging system as described in detail in Sec. 2.3. To reconstruct an envelope profile based on two phase profiles of neighboring phase values separated by Δf_z a total number of four individual 2D Fourier transforms is needed.

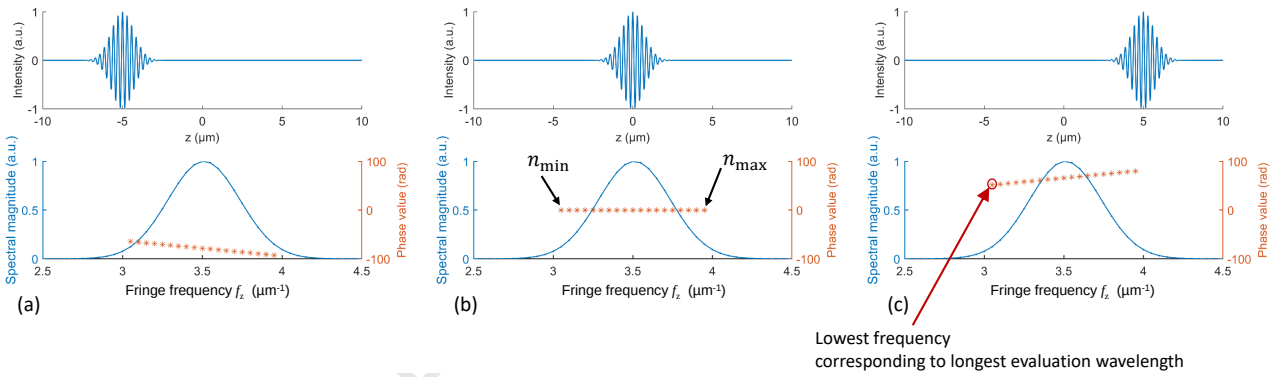

Figure 1. Simulated CSI signals (upper diagrams), corresponding spectral magnitudes and spectral phase values (lower diagrams): (a) signal position at $z = -5\,\mu$m, (b) signal position at $z = 0\,\mu$m, (c) signal position at $z = +5\,\mu$m.

The phase

$$\varphi(x,y) = q_z\, h_{\mathrm{ph}}(x,y). \tag{2}$$

of a measured phase object depends linearly on the angular fringe frequency and the reconstructed surface height function $h_{\mathrm{ph}}(x,y)$, which is a function of the coordinates x and y in the image plane. Once the phase function $\varphi(x,y)$ is known the surface height function also named phase profile can be reconstructed via

$$h_{\mathrm{ph}}(x,y) = \varphi(x,y)/q_z. \tag{3}$$

If a second phase function $\varphi_\Delta(x,y)$ is calculated for the angular fringe frequency $q_z + \Delta q_z$ the corresponding envelope profile results in

$$h_{\mathrm{env}}(x,y) = (\varphi_\Delta(x,y) - \varphi(x,y))/\Delta q_z. \tag{4}$$

Using the envelope information for fringe order determination results in the reconstructed height function:

$$h_{\mathrm{rec}}(x,y) = \mathrm{round}\left\{\frac{\varphi_\Delta(x,y) - \varphi(x,y)}{\Delta q_z\, \lambda_{\mathrm{eval}}/2}\right\} \frac{\lambda_{\mathrm{eval}}}{2} + \frac{\varphi(x,y)\,\lambda_{\mathrm{eval}}}{4\pi}, \tag{5}$$

which relates to a certain angular fringe frequency

$$q_z = q_{z,\mathrm{eval}} = \frac{4\pi}{\lambda_{\mathrm{eval}}}. \tag{6}$$

2.2 Simulation of interference signals

In order to simulate a phase function $\varphi(x, y)$ that considers the properties of the optical system, first the 2D Fourier transform of the field $U(x, y, q_z)$ related to the phase object needs to be calculated for the angular fringe frequency $q_{z,\mathrm{eval}}$.

This results in

$$\tilde{U}(q_x, q_y, q_z = q_{z,\mathrm{eval}}) = \frac{U_0}{A} \iint_{-\infty}^{+\infty} A(x, y)\, \mathrm{e}^{-\mathrm{i}q_{z,\mathrm{eval}}h(x,y)}\, \mathrm{e}^{-\mathrm{i}(q_x x + q_y y)} \mathrm{d}x\mathrm{d}y, \tag{7}$$

where A is the size of the illuminated area $A(x, y)$ and U_0 the field amplitude. According to the Kirchhoff or physical optics approximation q_x, q_y, q_z are the coordinates in the 3D spatial frequency domain called **q**-space throughout this paper. Note that Eq. (7) can be directly derived from the Kirchhoff integral of the scattered field. However, here the inclination factor known from the Kirchhoff approximation[14,23,24] is neglected, since in contrast to Kirchhoff scattering we assume a microscope with incoherent Koehler illumination and include all inclination factors in the 3D transfer function introduced below. If the electric field extends over an area A on the surface, which is large enough, the equivalent convolution with the 2D Fourier transform of $A(x, y)$ does not affect the final result. Hence,

$$\tilde{U}(q_x, q_y, q_z = q_{z,\mathrm{eval}}) \approx U_0 \iint_{-\infty}^{+\infty} \mathrm{e}^{-\mathrm{i}q_{z,\mathrm{eval}}h(x,y)}\, \mathrm{e}^{-\mathrm{i}(q_x x + q_y y)} \mathrm{d}x\mathrm{d}y \tag{8}$$

equals a 2D Fourier transform of the field in the object plane. The vector **q** in the spatial frequency domain comprises transverse spatial frequencies q_x and q_y and the axial spatial frequency q_z, which equals the angular fringe frequency. **q** represents the difference between the wave vector $\mathbf{k}_{\mathrm{s}}$ of the scattered light field and the wave vector $\mathbf{k}_{\mathrm{in}}$ of the incident wave:

$$\mathbf{q} = \mathbf{k}_{\mathrm{s}} - \mathbf{k}_{\mathrm{in}} = k_0 \begin{pmatrix} \sin(\theta_{\mathrm{s}})\cos(\phi_{\mathrm{s}}) - \sin(\theta_{\mathrm{in}})\cos(\phi_{\mathrm{in}}) \\ \sin(\theta_{\mathrm{s}})\sin(\phi_{\mathrm{s}}) - \sin(\theta_{\mathrm{in}})\sin(\phi_{\mathrm{in}}) \\ \cos(\theta_{\mathrm{in}}) + \cos(\theta_{\mathrm{s}}) \end{pmatrix}. \tag{9}$$

q is defined in terms of the wavenumber $k_0 = 2\pi/\lambda_0$ depending on the illumination wavelength λ_0 and the polar and azimuth angles θ_{in} and ϕ_{in} of the incident wave as well as the angles θ_{s} and ϕ_{s} of the scattered wave.[18] Note that Eq. (9) represents a generalized geometrical arrangement compared to the conventional Kirchhoff scattering geometry[24,25] since in a microscope a cone of incident wave vectors needs to be considered. The function $\tilde{U}(q_x, q_y, q_z = q_{z,\mathrm{eval}})$ is then multiplied by the 2D cross section of the 3D transfer function $\tilde{H}(q_x, q_y, q_z)$ introduced below corresponding to the axial spatial frequency $q_z = q_{z,\mathrm{eval}}$. This results in the complex function

$$\Delta\tilde{I}(q_x, q_y, q_z = q_{z,\mathrm{eval}}) = \tilde{U}(q_x, q_y, q_z = q_{z,\mathrm{eval}})\, \tilde{H}(q_x, q_y, q_z = q_{z,\mathrm{eval}}). \tag{10}$$

Inverse 2D Fourier transform of $\Delta\tilde{I}(q_x, q_y, q_z = q_{z,\mathrm{eval}})$ results in a complex interference intensity function

$$\Delta I(x, y, q_z = q_{z,\mathrm{eval}}) = \frac{1}{4\pi^2} \iint_{-\infty}^{+\infty} \Delta\tilde{I}(q_x, q_y, q_z = q_{z,\mathrm{eval}})\, \mathrm{e}^{\mathrm{i}(q_x x + q_y y)} \mathrm{d}q_x\mathrm{d}q_y. \tag{11}$$

This function represents the Fourier transform of the unbiased interference image stack with respect to the z-coordinate for a given angular spatial frequency $q_{z,\mathrm{eval}}$. The required phase function $\varphi(x, y)$ equals the phase of $\Delta I(x, y, q_z = q_{z,\mathrm{eval}})$, i.e.

$$\varphi(x, y, q_z = q_{z,\mathrm{eval}}) = \arctan\left(\frac{\mathrm{Im}\{\Delta I(x, y, q_z = q_{z,\mathrm{eval}})\}}{\mathrm{Re}\{\Delta I(x, y, q_z = q_{z,\mathrm{eval}})\}}\right). \tag{12}$$

From this phase function the corresponding phase profile for the angular fringe frequency $q_{z,\mathrm{eval}}$ will be reconstructed. Repeating the procedure for the fringe frequency $q_{z,\mathrm{eval}} + \Delta q_z$ results in a second phase profile. From these two phase profiles according to Eq. (4) an envelope profile can be derived. Of course, following this procedure for all discrete angular spatial frequencies appearing in the resulting discrete Fourier transform of a measured or simulated image stack with respect to the z-coordinate enables multiple reconstructions of phase and envelope profiles as mentioned before. Furthermore, Eq. (11) leads to a single fringe frequency component of an image stack. Hence, superposition of simulated sinusoidal interference signals for the whole set of fringe frequencies yields a simulated 3D interference image stack.

2.3 Three-dimensional transfer functions

The concept of 3D transfer functions is introduced in Figure 2. Figure 2 (a) shows a set of incident and scattered wave vectors $\mathbf{k}_\mathrm{i}$ and $\mathbf{k}_\mathrm{s}$, where the angle $\theta_\mathrm{max} = \arcsin(\mathrm{NA})$ limits the angles of incidence and the scattering angles due to the numerical aperture NA of the system. If the difference vectors $\mathbf{q}$ resulting from all possible combinations of $\mathbf{k}_\mathrm{i}$ and $\mathbf{k}_\mathrm{s}$ are plotted in a $\mathbf{q}$-coordinate system the Ewald limiting sphere[14] according to Figure 2 (b) results, which represents the typical umbrella shape. An analytical calculation of the optical 3D transfer function based on the correlation of two spherical caps belonging to the ensemble of contributing incident and scattered wave vectors is introduced elsewhere.[17] Since uniform intensity is assumed in the entrance and exit pupil planes, integration of this 3D TF along the q_z axis results in the well-known MTF of a diffraction limited imaging system. However, for piecewise continuous diffracting or tilted specular surfaces the intensity distribution in the exit pupil plane is no longer uniform and thus a slightly different 3D transfer function occurs.[18,19]

$$\begin{aligned}
\tilde{H}(q_\rho, q_z, k_0) &= \frac{q_z}{2k_0} \quad \text{for} \quad \mathbf{q} \in \mathrm{area}_1, \\
\tilde{H}(q_\rho, q_z, k_0) &= \left(1 - \frac{2}{\pi}\arccos\left(\frac{|\mathbf{q}|\left(q_z - k_0\sqrt{1-\mathrm{NA}^2}\right)}{q_\rho\sqrt{4k_0^2 - |\mathbf{q}|^2}}\right)\right)\frac{q_z}{2k_0} \quad \text{for} \quad \mathbf{q} \in \mathrm{area}_2, \\
\tilde{H}(q_\rho, q_z, k_0) &= 0 \qquad \text{elsewhere},
\end{aligned} \tag{13}$$

with $q_\rho = \sqrt{q_x^2 + q_y^2}$ representing the distance from the optical axis. Note that the factor $q_z/2k_0$ included in the 3D transfer function for both areas (1 and 2) equals the inclination factor derived from the Kirchhoff integral for plane wave scattering.[24] A 2D cross section in the $q_x q_z$-plane of a 3D transfer function for an NA of 0.9 and monochromatic light of 500 nm wavelength is plotted in Figure 2 (c). For a certain fringe frequency $q_{z,\mathrm{eval}}$ only the corresponding cross section of the 3D TF with respect to the $q_x q_y$-plane needs to be considered in Eq. (10). For example, the maximum lateral spatial frequency that can be resolved by an optical system corresponds to the q_z-position of maximum extend of the 3D transfer function along the q_x-axis, i.e. the minimum value of $q_{z,\mathrm{eval}}$, where the 3D TF is different from zero.[19] The 3D TF introduced so far describes the transfer characteristics of interference microscopes under monochromatic illumination given by the wavenumber $k_0 = 2\pi/\lambda_0$ and the central wavelength λ_0. However, CSI instruments commonly use broadband light sources such as light emitting diodes (LEDs). To take this into account, monochromatic 3D transfer functions must be weighted according to the wavenumber spectrum of the light source, the spectral sensititvity of the camera and the spectral transmittivity of the optical imaging system. Therefore, the polychromatic 3D TF results in

$$\tilde{H}(\mathbf{q}) = \int_0^\infty S(k_0)\ \tilde{H}(\mathbf{q}, k_0)\,\mathrm{d}k_0, \tag{14}$$

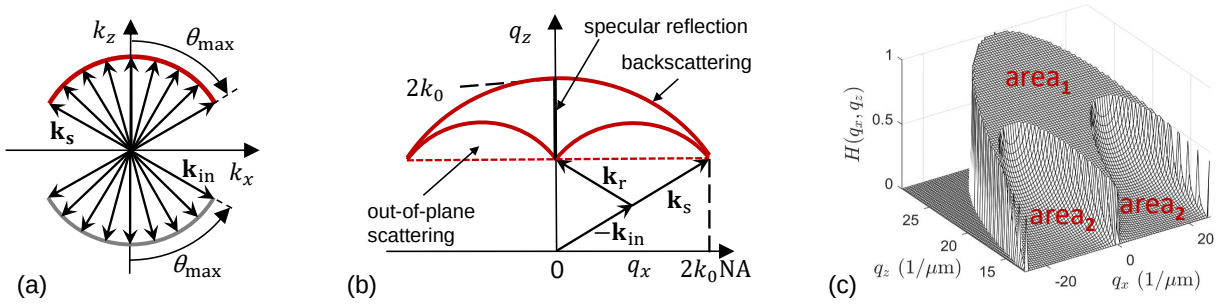

Figure 2. (a) Ewald sphere of an optical microscope generated by wavevectors $\mathbf{k}_{\text{in}}$ of incident light and $\mathbf{k}_{\text{s}}$ of scattered light, where the maximum angle θ_{max} is due to the NA of the system, (b) construction of the Ewald limiting sphere defining the $\mathbf{q}$-space, (c) two-dimensional cross section in the $q_x q_z$-plane of the monochromatic 3D transfer function of an interference microscope of NA = 0.9 for the wavelength $\lambda_0 = 500$ nm.

where $S(k_0)$ equals the overall spectral distribution. With respect to the transfer function $\tilde{H}(\mathbf{q}, k_0)$ it should be noticed that all Cartesian axes in $\mathbf{q}$-space scale with the wavenumber k_0. As a consequence, the 'wings' of the transfer function at high q_x and low q_z-values will be significantly shifted as the wavenumber changes and, as a consequence, the 3D TF will be blurred.[18] For the simulation results shown below we use Gaussian distributed wavenumbers according to spectral distribution:

$$S(k) = \frac{1}{\sqrt{\pi}\sigma_k}\, \mathrm{e}^{-(k-k_0)^2/\sigma_k^2}, \tag{15}$$

with the central wavenumber k_0 and the spectral full width at half maximum bandwidth

$$\text{FWHM} \approx 4\pi\sqrt{\ln 2}\,\sigma_k/k_0^2. \tag{16}$$

According to Figure 2 (b) specularly reflected light contributes to the 3D spatial frequency representation at

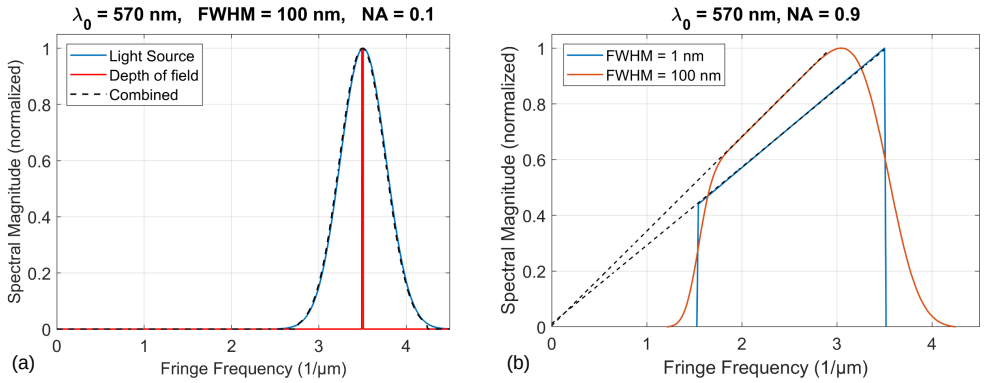

Figure 3. Spectra of simulated CSI signals appearing at a mirror-like object (a) for a broad spectral bandwidth (FWHM = 100 nm) of the light emitted by the light source and a low NA system (NA = 0.1) resulting in a high depth of field, (b) for a high NA system (NA = 0.9) resulting in a low depth of field and both, nearly monochromatic light as well as broad bandwidth light (FWHM = 100 nm).

$q_x = 0, q_y = 0$. Hence, $\tilde{H}(q_x = 0, q_y = 0, q_z)$ is related to the transfer characteristics of a plane mirror depending on the fringe frequency $f_z = q_z/2\pi$. Figure 3 (a) shows such a fringe frequency distribution for an imaging system of low NA = 0.1. The blue Gaussian curve represents a Gaussian spectral distribution with FWHM = 100 nm. The red spectral peak belongs to the rather long depth of field related to a long sinusoidal interference signal

of the center wavelength $\lambda_0 = 570$ nm. The spectral bandwidth of the light source dominates the spectral bandwidth of the interference signal. A different situation occurs for a system of high NA as it is shown in Figure 3 (b) for NA = 0.9. In this case, even for a narrow bandwidth of 1 nm a broad spectral distribution results, that follows the well-known ramp shape[26,27] in accordance with the 3D transfer function given in Eq. (13). For a larger FWHM of 100 nm the spectral distribution is broadened and the flanks are rounded due to the Gaussian wavenumber distribution, but still the spectral contributions due to the limited depth of field dominate and in the region $2\,\mu\text{m}^{-1} < f_z < 3\,\mu\text{m}^{-1}$ the ramp shape can be recognized.

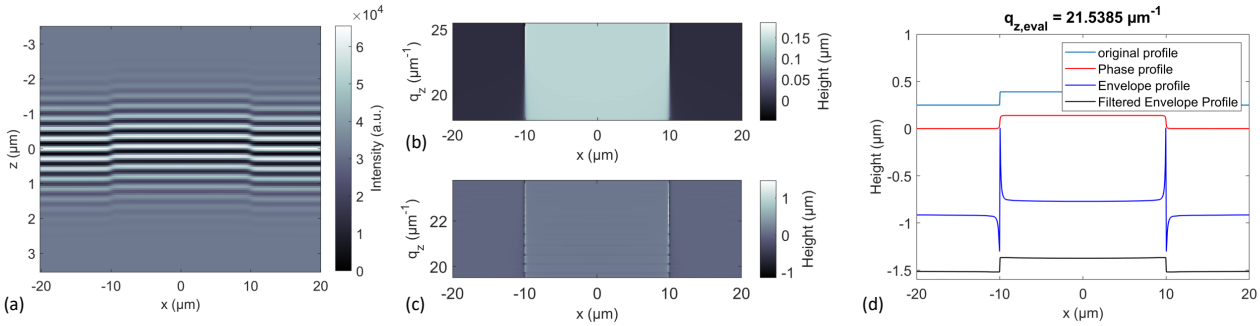

Figure 4. (a) Interference signals in the xz-plane related to a single rectangular plateau of 20 µm width and 140 nm height for a CSI instrument of NA = 0.3, $\lambda_0 = 570$ nm and FWHM = 80 nm, (b) and (c) reconstructed height profiles depending on the angular fringe frequency q_z using either phase (b, Eq. (3)) or envelope analysis (c, Eq. (4)), (d) reconstructed surface profiles for $q_{z,\text{eval}} = 21.5385\ \mu\text{m}^{-1}$.

3. SIMULATION RESULTS

A further significant reduction of the computational effort can be achieved, if the input surface $h(x, y)$ is translational invariant with respect to the y coordinate, i.e. $h(x, y) = h(x)$. In this case $q_y = 0$ in Eq. (9) and only the $q_x q_z$-plane needs to be considered for the scattered light field. Consequently, according to Eq. (10) only the 2D cross section $H(q_x, q_z)$ of the 3D transfer function becomes relevant. Hence, the simulation of a phase profile for a certain angular fringe frequency $q_{z,\text{eval}}$ requires only two one-dimensional fast Fourier transforms. To simulate an envelope profile twice the computational effort is needed as mentioned above.

Figure 4 (a) shows interference signals in the xz-plane related to a single rectangular plateau of 20 µm width and 140 nm height for a CSI instrument of NA = 0.3, $\lambda_0 = 570$ nm and FWHM = 80 nm. Figures 4 (b) and (c) display reconstructed height profiles for different angular fringe frequencies q_z using either phase (Figure 4 (b), Eq. (3)) or envelope analysis (Figure 4 (c), Eq. (4)). For $q_z < 20\ \mu\text{m}^{-1}$ the phase profiles are blurred at the edges, whereas the envelope profiles show strong batwings for certain q_z-values as it is shown in Figure 4 (d) for $q_{z,\text{eval}} = 21.5385\ \mu\text{m}^{-1}$. Due to the redundancy of the profiles evaluated at different fringe frequencies, median filtering can be applied to the columns of Figure 4 (c) resulting in the filtered envelope profile (black curve in Figure 4 (d)), where the batwings disappear.

In Figure 5 reconstructed sinusoidal profiles of 3.6 µm period and 200 nm amplitude assuming a CSI instrument of NA = 0.55, $\lambda_0 = 570$ nm and FWHM = 100 nm are shown. The profiles obtained for different evaluation wavelength again exhibit the strong dependence on $q_{z,\text{eval}} = 4\pi/\lambda_{\text{eval}}$. While the red curves representing the unwrapped phase profiles are less affected, the envelope profiles show the typical slope effect,[7] which leads to phase jumps in Figures 5 (a) and (d) if the fringe order of the phase profile (black curves) is obtained from the envelope profile. The best reconstruction is achieved for the phase profile according to Figure 5 (c) for an evaluation wavelength of 613 nm.

Figure 6 depicts reconstructed sinusoidal profiles for an input sinusoidal surface of 0.3 µm period and 30 nm amplitude simulated for a CSI instrument of NA = 0.9, $\lambda_0 = 450$ nm and FWHM = 80 nm. Single profiles for the three different values $q_{z,\text{eval}} = 27.5$, 20 and 16 µm^{-1} marked by the dashed red lines in Figure 6 are plotted in Figure 7. Even though the input profile is no longer resolved in Figure 7 (a) for $\lambda_{\text{eval}} = 457$ nm, the profile is

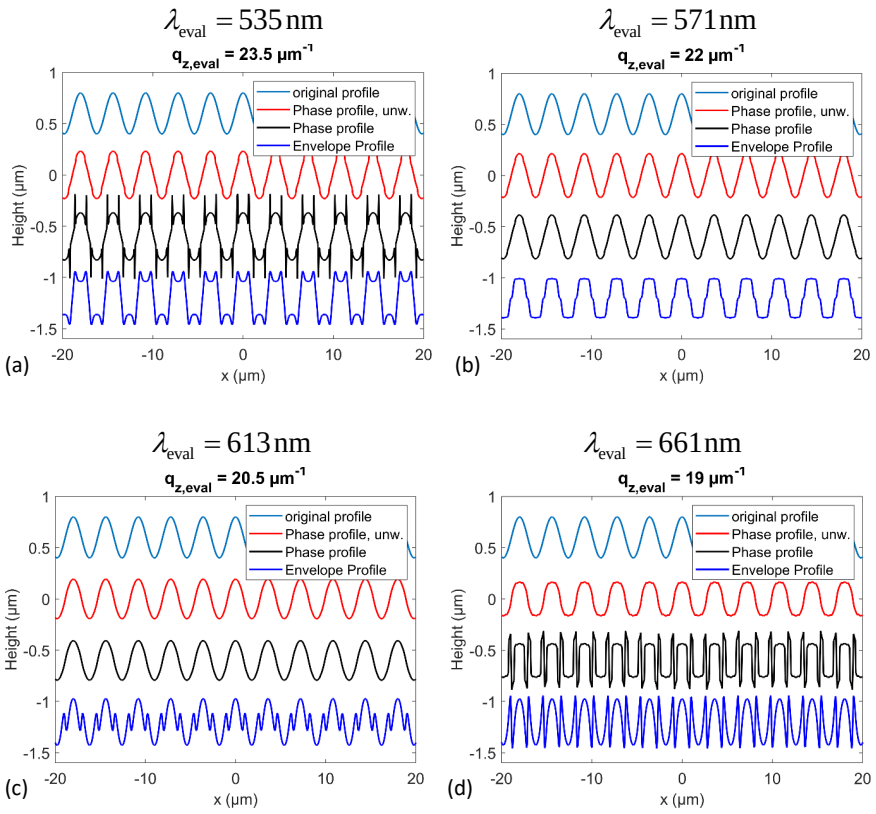

Figure 5. Reconstructed sinusoidal profiles of 3.6 µm period and 200 nm amplitude assuming a CSI instrument of NA = 0.55, λ_0 = 570 nm and FWHM = 100 nm, the profiles are obtained for evaluation wavelengths λ_{eval} of 535 nm (a), 571 nm (b), 613 nm (c) and 661 nm (d).

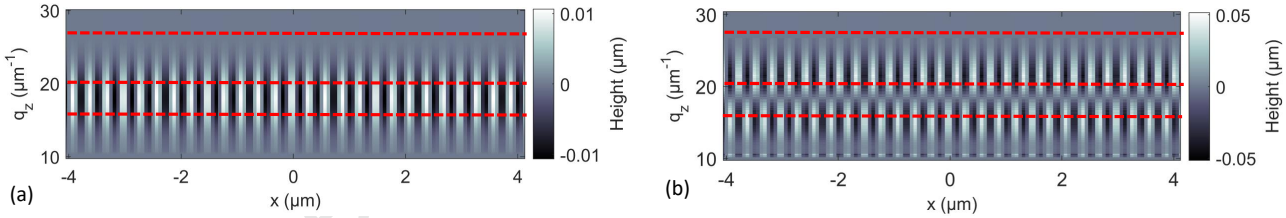

Figure 6. Reconstructed sinusoidal profiles for an input surface of 0.3 µm period and 30 nm amplitude simulated for a CSI instrument of NA = 0.9, λ_0 = 450 nm and FWHM = 80 nm, (a) phase profiles depending on the angular fringe frequency q_z, (b) envelope profiles depending on the angular fringe frequency q_z.

laterally resolved in Figures 7 (b) and (c) for significantly longer evaluation wavelengths of λ_{eval} = 628 nm and 785 nm, respectively. However, in Figure 7 (b) the envelope profile is inverted, what can be seen also in Figure 6 (b), whereas the sign of the envelope profile is correct in Figure 7 (c). In both cases, Figures 7 (b) and (c), the amplitudes of the reconstructed phase profiles are much too small. These effects were already observed in experimental results and stem from the limited lateral resolution of the instrument.[20,28]

4. CONCLUSION

In this contribution we introduce a Universal Fourier Optics (UFO) model that provides fast simulations of CSI measurement results and prediction of systematic measurement errors. The model holds under the assumptions

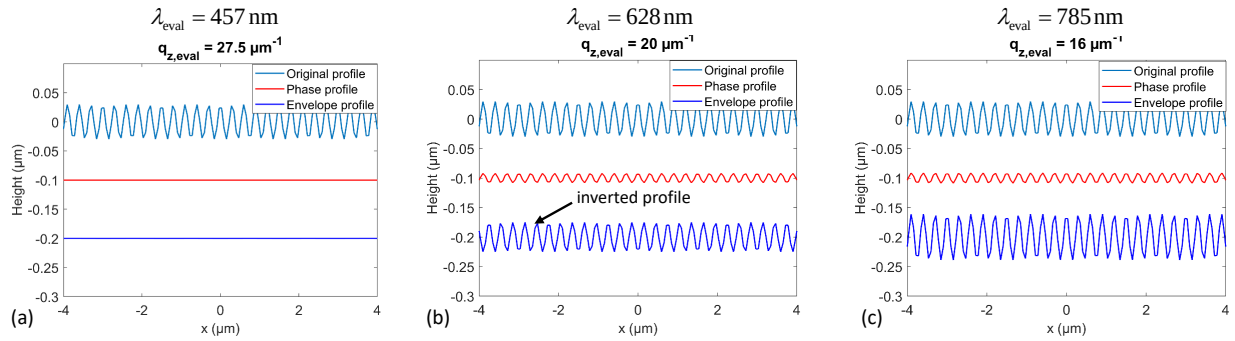

Figure 7. Reconstructed sinusoidal profiles according to Figure 6 for the evaluation wavelengths $\lambda_{eval} = 457$ nm (a), 628 nm (b) and 785 nm (c).

of the Kirchhoff or physical optics approximation and multiplies the Fourier transformed light field on the surface of a phase object by the corresponding cross-section of the 3D transfer function, which is calculated analytically.

Due to its computational efficiency the UFO model allows not only the reconstruction of phase and envelope profiles for single, preselected fringe frequencies. If simulations are performed for different fringe frequencies following the spectral distribution of incident light and considering the spectral broadening due to the numerical aperture of the CSI instrument the model provides a full CSI interference image stack after a few seconds runtime of a Matlab coded program on an Intel Core i7-9700K CPU. From such simulations most suitable parameters for surface profile reconstruction can be obtained in order to reduce sytematic deviations between measured and input profiles.

ACKNOWLEDGMENTS

This work was supported by the European Metrology Programme for Innovation and Research (EMPIR) project [TracOptic, 20IND07].

REFERENCES

[1] Malacara, D., [*Optical Shop Testing*], John Wiley & Sons, Inc, Hoboken, NJ, USA (2007).
[2] Abdulhalim, I., "Spatial and temporal coherence effects in interference microscopy and full-field optical coherence tomography," *Annalen der Physik* **524**(12), 787–804 (2012).
[3] Harasaki, A. and Wyant, J. C., "Fringe modulation skewing effect in white-light vertical scanning interferometry," *Applied Optics* **39**(13), 2101–2106 (2000).
[4] Xie, W., Lehmann, P., Niehues, J., and Tereschenko, S., "Signal modeling in low coherence interference microscopy on example of rectangular grating," *Optics Express* **24**(13), 14283–14300 (2016).
[5] Pahl, T., Hagemeier, S., Hüser, L., Xie, W., and Lehmann, P., "Two-dimensional modelling of systematic surface height deviations in optical interference microscopy based on rigorous near field calculation," *Journal of Modern Optics* **67**(11), 963–973 (2020).
[6] Pahl, T., Hagemeier, S., Künne, M., Di Yang, and Lehmann, P., "3D modeling of coherence scanning interferometry on 2D surfaces using FEM," *Optics Express* **28**(26), 39807–39826 (2020).
[7] Gao, F., Leach, R., K., Petzing, J., and Coupland, J. M., "Surface measurement errors using commercial scanning white light interferometers," *Measurement Science and Technology* **19**(1), 015303 (13pp.) (2008).
[8] Sheppard, C. J. R., "Imaging of random surfaces and inverse scattering in the kirchhoff approximation," *Waves in Random Media* **8**(1), 53–66 (1998).
[9] Coupland, J., Mandal, R., Palodhi, K., and Leach, R., "Coherence scanning interferometry: linear theory of surface measurement," *Applied Optics* **52**(16), 3662–3670 (2013).
[10] Su, R., Coupland, J., Sheppard, C., and Leach, R., "Scattering and three-dimensional imaging in surface topography measuring interference microscopy," *JOSA A* **38**(2), A27–A42 (2021).

[11] Su, R., Thomas, M., Liu, M., Drs, J., Bellouard, Y., Pruss, C., Coupland, J., and Leach, R., "Lens aberration compensation in interference microscopy," *Optics and Lasers in Engineering* **128**, 106015 (2020).
[12] Su, R., Thomas, M., Leach, R., and Coupland, J., "Effects of defocus on the transfer function of coherence scanning interferometry," *Optics Letters* **43**(1), 82–85 (2018).
[13] Su, R. and Leach, R., "Physics-based virtual coherence scanning interferometer for surface measurement," *Light: Advanced Manufacturing* **2**(1), 1–16 (2021).
[14] Born, M. and Wolf, E., [*Principles of Optics*], Cambridge University Press, Cambridge (UK) (1999).
[15] de Groot, P. J. and Colonna de Lega, X., "Fourier optics modeling of interference microscopes," *JOSA A* **37**(9), B1–B10 (2020).
[16] Lehmann, P., Künne, M., and Pahl, T., "Analysis of interference microscopy in the spatial frequency domain," *Journal of Physics: Photonics* **3**(1), 014006 (2021).
[17] Lehmann, P. and Pahl, T., "Three-dimensional transfer function of optical microscopes in reflection mode," *Journal of Microscopy* **284**(1), 45–55 (2021).
[18] Lehmann, P., Hagemeier, S., and Pahl, T., "Three-dimensional transfer functions of interference microscopes," *Metrology* **1**(2), 122–141 (2021).
[19] Lehmann, P., Hüser, L., Stelter, A., and Kusserow, T., "Lateral resolution enhanced interference microscopy using virtual annular apertures," *Journal of Physics: Photonics* **5**(1), 015001 (2023).
[20] Lehmann, P., Tereschenko, S., Allendorf, B., Hagemeier, S., and Hüser, L., "Spectral composition of low-coherence interferograms at high numerical apertures," *Journal of the European Optical Society-Rapid Publications* **15**(1), 3775 (2019).
[21] de Groot, P. J. and Deck, L. L., "Surface profiling by analysis of white light interferograms in the spatial frequency domain analysis of white light interferograms," *Journal of Modern Optics* **42**(2), 389–401 (1994).
[22] de Groot, P., Colonna de Lega, X., Su, R., Coupland, J., and Leach, R., "Modeling of coherence scanning interferometry using classical fourier optics," *Opt. Eng.* **60**(10), 104106–1–104106–19 (2021).
[23] Goodman, Joseph, W., [*Introduction to Fourier Optics*], Roberts, Englewood (Massachusetts) (2005).
[24] Ogilvy, J. A., "Wave scattering from rough surfaces," *Rep. Prog. Phys.* **50**, 1553–1608 (1987).
[25] Beckmann, P. and Spizzichino, A., [*The scattering of electromagnetic waves from rough surfaces*], Artech House, Norwood (Massachusetts) (1987).
[26] de Groot, P. and de Lega, X. C., "Signal modeling for low-coherence height-scanning interference microscopy," *Applied Optics* **43**(25), 4821–4830 (2004).
[27] Sheppard, C. and Larkin, K. G., "Effect of numerical aperture on interference fringe spacing," *Applied Optics* **34**(22), 4731–4734 (1995).
[28] Lehmann, P., Xie, W., Allendorf, B., and Tereschenko, S., "Coherence scanning and phase imaging optical interference microscopy at the lateral resolution limit," *Optics Express* **26**(6), 7376–7389 (2018).

P. Lehmann, T. Pahl, J. Riebeling "Universal Fourier optics model for virtual coherence scanning interferometers" SPIE Proceedings 12619, Modeling Aspects in Optical Metrology IX, 1216190O, (August 10, 2023).

https://doi.org/10.1117/12.2673292